

Magnetic excitons in non-magnetic CrCl₃

Georgy Ermolaev^{1†}, Tagir Mazitov^{2†}, Anton Minnekhanov¹, Arslan Mazitov¹, Gleb Tselikov¹, Aleksandr Slavich¹, Alexey P. Tsapenko¹, Mikhail Tatmyshevskiy², Mikhail Kashchenko², Nikolay Pak¹, Andrey Vyshnevyy¹, Alexander Melentev², Elena Zhukova², Dmitriy Grudin¹, Junhua Luo³, Ivan Kruglov¹, Aleksey Arsenin¹, Sangen Zhao^{3,4*}, Kostya S. Novoselov^{5,6,7*}, Andrey Katanin^{2*}, Valentyn S. Volkov^{1*}

¹*Emerging Technologies Research Center, XPANCEO, Internet City, Emmay Tower, Dubai, United Arab Emirates*

²*Moscow Center for Advanced Studies, Kulakova str. 20, Moscow, 123592, Russia*

³*State Key Laboratory of Structural Chemistry, Fujian Institute of Research on the Structure of Matter, Chinese Academy of Sciences, Fuzhou, Fujian, 350002 P. R. China*

⁴*Quantum Science Center of Guangdong–Hong Kong–Macao Greater Bay Area (Guangdong), Shenzhen 518045, P. R. China*

⁵*National Graphene Institute (NGI), University of Manchester, Manchester, M13 9PL, UK*

⁶*Department of Materials Science and Engineering, National University of Singapore, Singapore, 03-09 EA, Singapore*

⁷*Institute for Functional Intelligent Materials, National University of Singapore, 117544, Singapore, Singapore*

[†]These authors contributed equally to this work

*Correspondence should be addressed to e-mail: zhaosangen@quantumsc.cn, kostya@nus.edu.sg, andrey.katanin@gmail.com, and vsv@xpanceo.com

Abstract

Van der Waals (vdW) materials, with their unique combination of electronic, optical, and magnetic properties, are emerging as promising platforms for exploring excitonic phenomena. Thus far, the choice of materials with exceptional excitonic response has been limited to two-dimensional (2D) configurations of vdW materials. At the same time, large interlayer distance and the possibility to create a variety of heterostructures offers an opportunity to control the dielectric screening in van der Waals heterostructures and van der Waal 3D materials, thus engineering the excitonic properties. Here, we reveal that bulk vdW crystal CrCl_3 answers this quest with a record exciton binding energy of 1.64 eV owing to a delicate interplay of quasi-2D electronic confinement and short-range magnetic correlations. Furthermore, we observe colossal binding energies in vdW crystals NbOCl_2 (0.66 eV) and MoCl_3 (0.35 eV) and formulate a universal exciton binding energy dependence on bandgap for 2D and 3D vdW materials. Hence, our findings establish a fundamental link between the layered structure of vdW materials and their excitonic properties.

Keywords: excitons, binding energy, 2D materials, magnetism, optical properties.

Introduction

Excitons, the bound state of electrons and holes, have led to myriad phenomena and applications, particularly with the emergence of two-dimensional (2D) materials^{1,2}. These materials demonstrate giant exciton binding energy due to their 2D nature, which allows their efficient use in photodetectors³, light-emitting diodes⁴, photovoltaics⁵, quantum communication and computing^{6,7}, valleytronics⁸, and exciton-polariton transport⁹. In light of this, an intriguing question emerges: if layered materials, essentially stacks of monolayers, also exhibit these fundamental excitonic features, can we anticipate equally enormous binding energies in bulk layered materials? This hypothesis suggests that the unique excitonic behavior observed in 2D materials might extend to their bulk counterparts, potentially opening new avenues for optoelectronics and quantum technologies^{6,10}. Numerous groups¹¹⁻¹³ tried to answer this question by investigating bulk transition metal dichalcogenides, but their findings are controversial. This controversy stems from the experimental difficulties arising from the overlapping of excitonic peaks with quasiparticle bandgap^{14,15}, which makes the task of measuring binding energy a challenging problem. Hence, one needs clearly separated excitons from bandgap to determine their binding energy unequivocally. In this regard, the new family of magnetic halogen-based layered materials, including CrCl_3 , CrBr_3 , and CrI_3 , is a promising platform to resolve this challenge since, for them, theory predicts individual excitonic peaks even in the bulk form^{16,17}. Moreover, their pronounced magnetic properties¹⁸⁻²⁰ may positively affect their excitonic response. Therefore, a van der Waals (vdW) crystal with giant exciton binding energy originating from magnetic order is highly desirable for developing exciton-based devices.

In this work, we experimentally and theoretically observed giant exciton binding energy in bulk CrCl_3 . Our results demonstrate that excitons in CrCl_3 originate from short-order magnetic correlations even at room temperature despite the small Curie temperature of about 20 K¹⁹⁻²¹. We emphasize that giant exciton binding energy in this material is due to the quasi-two-dimensionality of its electronic and magnetic properties. Furthermore, we found other vdW crystals, NbOCl_2 and MoCl_3 , with similarly large exciton binding energy, which is also related to their layered structure. Our work exposes a non-trivial link between electronic, magnetic, and optical properties and shows that halogen-based vdW materials are a promising material platform for comprehensive exciton physics and applications.

Results

Excitons in different dimensionalities

In 2D materials (Figure 1a), excitons exhibit significantly enhanced binding energies compared to their three-dimensional (3D) counterparts (Figure 1b)^{14,15}. This phenomenon can be attributed to several key factors intrinsic to the reduced dimensionality. Firstly, the reduced dielectric screening in 2D materials plays a crucial role. In 3D material, the dielectric permittivity is relatively high, leading to effective screening of the Coulomb interaction between the electron and hole that form the exciton. However, in the 2D case, the dielectric environment has a relatively low dielectric screening, facilitating the Coulomb interaction (Figure 1a). Secondly, the quantum confinement effect in 2D materials enhances excitonic binding energy. Additionally, in 2D, Coulomb potential modifies from the Gauss $1/r$ law to the Rytova–Keldysh form¹⁵, further strengthening electron-hole binding. In this context, the most interesting case for excitons is layered/vdW materials (Figure 1c), where excitons are also confined within a single plane, sharing similarities with 2D material (Figure 1a). At the same time, layered/vdW materials have a relatively strong dielectric response, making it look like a 3D case (Figure 1b). Consequently, excitons in layered materials should share properties from both 2D and 3D situations with an intermediate value of binding energies. Naively, one could expect that vdW crystals with a relatively large dielectric response ($\epsilon \sim 15$) would exhibit a moderate binding energy, while for the relatively small dielectric response ($\epsilon \sim 5$), one can anticipate a colossal binding energy in vdW materials comparable to 2D materials.

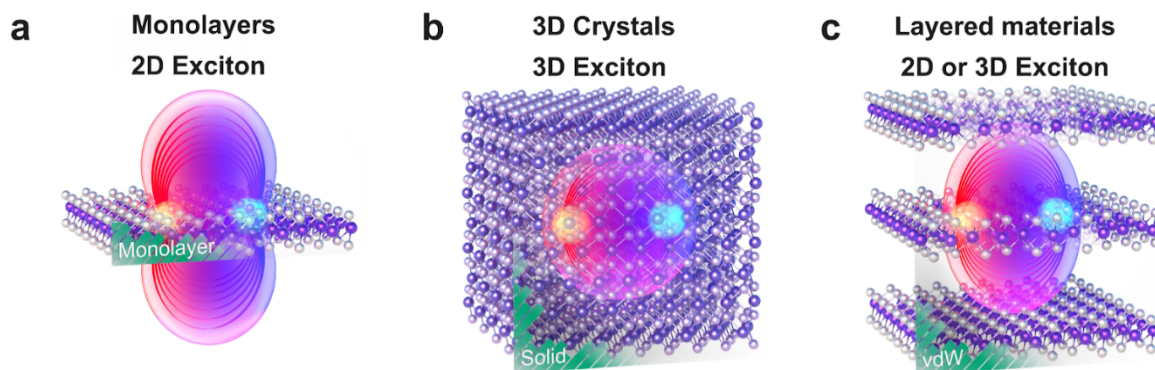


Figure 1. Real-space representations of excitons in different dimensions. **a**, Exciton in 2D material. **b**, Exciton in 3D material. **c**, Exciton in layered bulk materials, where it can demonstrate both 2D and 3D features.

Observation of CrCl_3 excitons

To validate the proposed concept, we first focus on CrCl_3 excitons, which recently received considerable attention^{16,17,19,22}. In layered form, CrCl_3 is a vdW monoclinic crystal with the following lattice parameters: $a = 0.59588$ nm, $b = 1.032206$ nm, $c = 0.61138$ nm, $\alpha = 90^\circ$, $\beta = 108.495^\circ$, and $\gamma = 90^\circ$ (Figure 1a) in the $C2/m$ phase observed at room temperature²³. Its reduced crystal symmetry generally leads to a dielectric tensor of non-diagonal form with wandering principal optical axes. Fortunately, its in-plane optical anisotropy is negligible (Supplementary Note 1), allowing us to treat CrCl_3 as an optically uniaxial system with dielectric tensor matrix $\text{diag}(n_{ab}+ik_{ab}, n_{ab}+ik_{ab}, n_c+ik_c)$, where n_{ab} , n_c and k_{ab} , k_c are refractive indices and extinction coefficients along ab -plane and c -axis, respectively.

To obtain anisotropic optical constants of CrCl₃, we measured reflectance (Figure 2a), transmittance (Figure 2b), and ellipsometry (Supplementary Note 2) spectra of exfoliated CrCl₃ flake on the glass substrate. Notably, the resulting spectra demonstrate pronounced Fabry–Perot resonances with apparent dips around 1.7 eV and 2.3 eV in transmittance, indicating the presence of excitons (Figure 2c). For simultaneous fitting of reflectance, transmittance, and ellipsometry spectra, we leverage standard for layered materials Tauc–Lorentz oscillators approach for in-plane optical constants and a Cauchy model for out-of-plane optical constants of CrCl₃ (Supplementary Note 3)⁹. The resulting refractive indices and extinction coefficients are displayed in Figure 2d and Figure 2e, respectively. In accordance with theoretical studies¹⁷, which predict A- and B-excitons positions at 1.78 eV and 2.51 eV, respectively, we observe them at $E_A = 1.67$ eV and $E_B = 2.28$ eV (the inset in Figure 2e). More importantly, the bandgap of CrCl₃ is well separated from excitonic peaks, enabling unambiguous determination of bandgap position $E_g = 3.31$ eV (Figure 2e) and the corresponding excitons binding energies $E_A^{\text{binding}} = E_g - E_A = 1.64$ eV and $E_B^{\text{binding}} = E_g - E_B = 1.03$ eV. To the best of our knowledge, these values are the largest among all experimentally measured excitonic materials, even compared to previous record-holders monolayers^{14,15} MoS₂ and WS₂ with $E_A^{\text{binding}} = 0.45$ eV and $E_B^{\text{binding}} = 0.32$ eV, respectively.

Apart from intriguing linear optical properties, excitons in CrCl₃ demonstrate distinctive photoluminescence (PL), as seen in Figures 2f-h. Unlike the isotropy of in-plane optical constants (Supplementary Note 1), PL exhibits an anisotropic response (Figures 2e-f), allowing us to determine the preferential orientation of the fundamental exciton with respect to the crystallographic axes. It turns out that the fundamental exciton in CrCl₃ is rotated by 48° with respect to the a-axis (Supplementary Note 4). Furthermore, at both standard excitation wavelengths—532 nm (Figure 2f) and 785 nm (Figure 2g)—CrCl₃ displays a similar PL pattern (Figure 2h), even though they correspond to different excitons: the corresponding energies 2.33 eV and 1.58 eV coincide well with the B- (2.28 eV) and A-exciton (1.67 eV) positions, respectively. This behavior suggests that the B-exciton relaxes to the A-exciton before the radiative recombination. In addition to PL, CrCl₃ demonstrates promising waveguiding properties, with a propagation length of 70 μm for exciton–polaritons, which is an order of magnitude larger than that of traditional MoSe₂ exciton–polaritons with a propagation length of 2.5 μm (Supplementary Note 5).

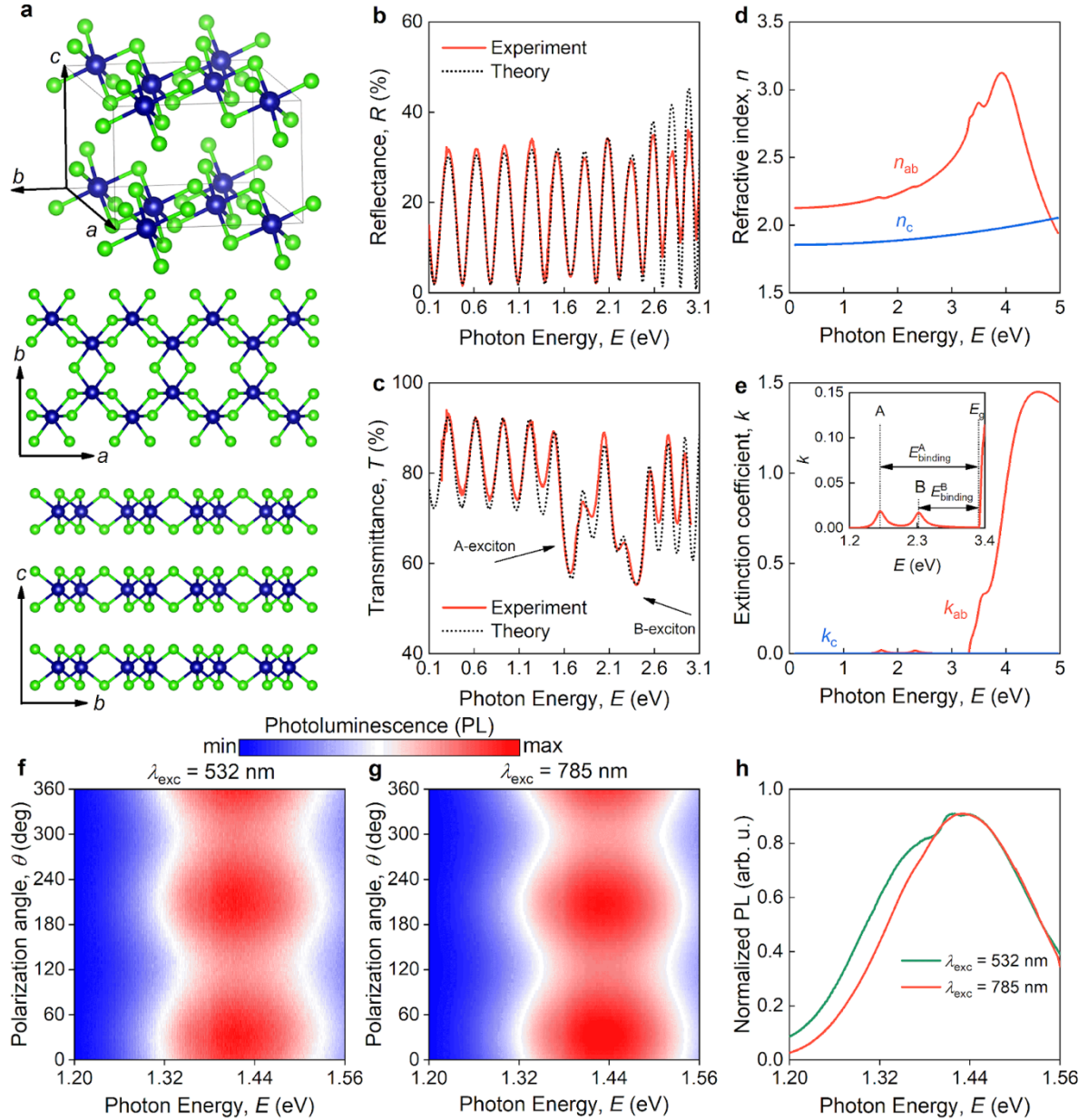


Figure 2. Excitonic optical properties of CrCl_3 . **a**, Crystal structure of CrCl_3 : three-dimensional view of the unit cell (top), view along the c -axis (middle), view along the a -axis (bottom). **b**, Reflectance and **c**, transmittance spectra of 945-nm thick CrCl_3 flake. **d**, Anisotropic refractive index of CrCl_3 . **e**, Anisotropic extinction coefficient of CrCl_3 . The inset shows the spectral region with excitons. Photoluminescence spectra of CrCl_3 for **f**, 532 nm and **g**, 785 nm excitation wavelengths. **h**, Averaged over polarization angles normalized photoluminescence spectra of CrCl_3 .

Short-range magnetic nature of CrCl_3 excitons

As mentioned above, CrCl_3 is not magnetically ordered at room temperature²⁰ and becomes ferromagnetic only at temperatures of about 20 K. However, we might expect short-range magnetic correlations at room temperature, which may have profound effects on the appearance of excitons. To estimate the strength of these correlations, we have performed a DFT+DMFT calculation with subsequent evaluation of non-local static susceptibility²⁴, which we then decompose according to the contributions of various neighbors (see Supplementary Note 6 for more details). The calculated contributions from the nearest and next-nearest neighboring Cr sites inside CrCl_3 layers and the nearest neighbours between the vdW layers are shown in Figure 3a. The obtained contributions are all positive, which indicates ferromagnetic short-range order, in agreement with the onset of

ferromagnetic long-range order with lowering the temperature. The key feature is a rapid increase of the non-local susceptibility with decreasing temperature. At room temperature, the value of the in-plane nearest-neighbor contribution (per neighbor) is already $\chi_{nn} \sim 12 \text{ eV}^{-1}$, which, in combination with the on-site Coulomb repulsion $U \sim 3 \text{ eV}$, provides a substantial bare non-local interaction $U^2\chi_{nn} \sim 100 \text{ eV}$, characterizing a strong short-range magnetic order of CrCl_3 . Although the vertex and non-local self-energy corrections can suppress this contribution, it is expected to be sufficient to induce a quasi-splitting of the electronic spectrum, similar to that suggested previously in the metallic phase^{25,26}. The correlations of the nearest Cr-atoms in neighboring layers are much smaller than between atoms within the same layer, suggesting the quasi-two-dimensionality of this material.

To confirm the decisive role of magnetic correlations in the formation of excitons in CrCl_3 , we have also measured the temperature dependence of PL response. Given the rapid change of non-local spin susceptibility with temperature (Figure 3a), we expect a similar dependence of exciton photoluminescence (PL). Indeed, PL intensity significantly increases with the cooling of CrCl_3 , as seen in Figure 3b. However, even in the classical case, temperature T affects the PL intensity I following Arrhenius law $I(T) = I_0/(1+C \exp[-E_a/(k_B T)])$, where I_0 is PL intensity at low temperatures, C is a phenomenological constant, k_B is a Boltzmann constant, and E_a is an activation energy^{27,28}. Figure 3c shows that the Arrhenius law describes the PL temperature dependence only for high temperatures, where magnetic correlations are not quite important due to smallness of the non-local susceptibility (Figure 3a). Considering Figure 3a and assuming that the low-temperature intensity I_0 scales with temperature according to the extrapolated temperature dependence of the obtained non-local spin susceptibility, we arrive at an agreement of the experiment and theory also in the intermediate temperature range (Figure 3c). Therefore, this result confirms the magnetic origin of excitons in CrCl_3 .

To study the the optical properties of CrCl_3 , and especially the excitonic properties and dielectric response in the presence of magnetic correlations, we further performed GW calculation with spin-orbit interaction extended with a Bethe–Salpeter equation (BSE) formalism to capture the two-particle (electron-hole) interactions (Figures 3b-c). Following our DFT+DMFT calculations, and other recent studies^{16,20} of the CrCl_3 system, we consider the ferromagnetic order, which describes in the above-mentioned ab initio calculations the effect of short-range magnetic correlations (the results for other magnetic configurations are presented in Supplementary Note 7). In the long-wavelength limit, our GW results on refractive index and extinction coefficient (Figure 3b) demonstrate very good quantitative agreement with the experimental results obtained with ellipsometry. However, due to the lack of electron-hole description in the GW approach, the agreement in the short-wavelength region could be improved. Indeed, this picture changes quite noticeably when taking the electron-hole interaction into account within BSE formalism (Figure 3c). Our results on the position of the A exciton ($E_A = 1.70 \text{ eV}$) are aligned perfectly with the experimental results obtained in this work (Figure 3c). The B exciton is less pronounced in BSE and can be noticed by the inflection of the absorbance curve around $E_B = 2.40 \text{ eV}$, which is slightly higher than the experimental result $E_B = 2.28 \text{ eV}$ (Figure 3c). Additionally, both results agree on a quantitative level with earlier experimental^{29,30} and theoretical^{16,17} works (Figure 3d). Besides, in our calculations, we account for spin-orbit interaction, which allows us to achieve an agreement with the experimental data for considered ferromagnetic order. In contrast, the previous study¹⁷ considered antiferromagnetic order without spin-orbit interaction, whereas the magnetic state in reference¹⁶ was not specified. Notably, in the presence of the spin-orbit interaction, excitons are absent in paramagnetic and antiferromagnetic ordered phases (see Supplementary Note 7), which also confirms the importance of short-range ferromagnetic order

for exciton formation in CrCl_3 . Thus, our results demonstrate a strong connection between optics and magnetism, where even the direction of the magnetic moment can affect the excitonic picture of the optical response.

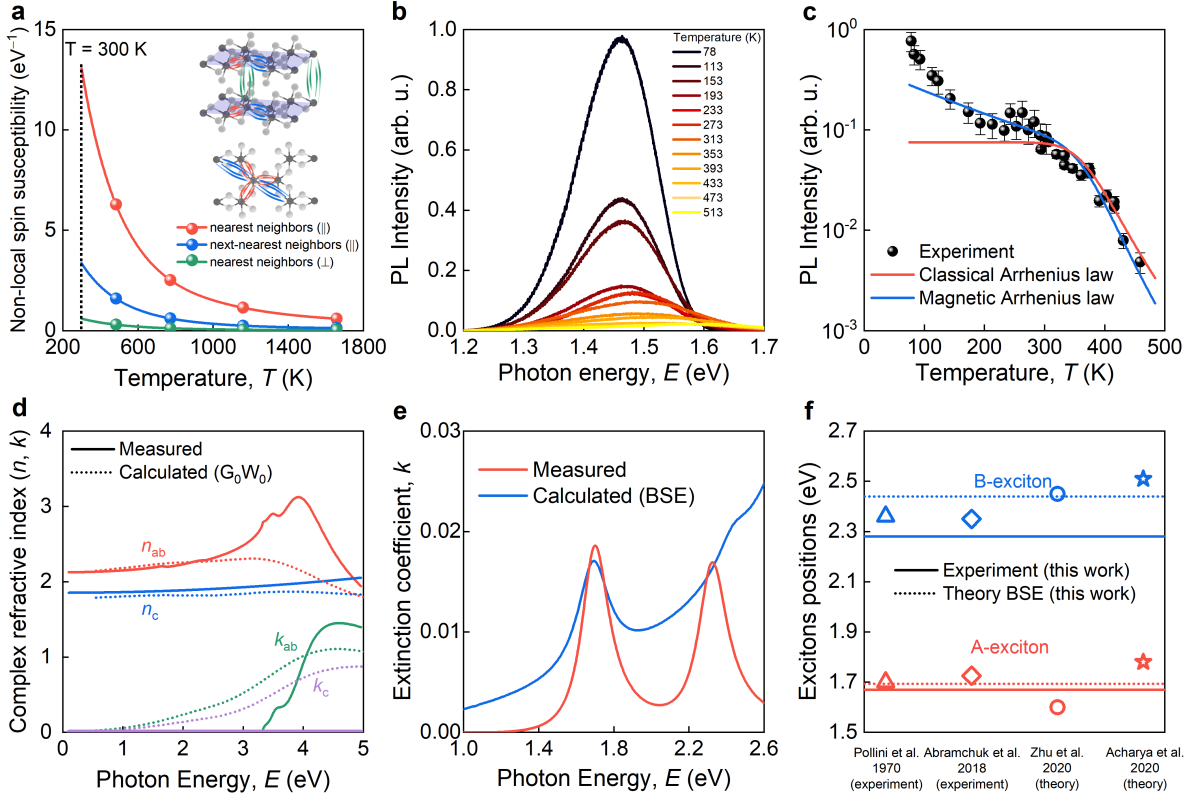


Figure 3. Theory of magnetic excitons in CrCl_3 . **a**, Contributions (per neighbor) to the non-local spin susceptibility from the nearest (red line, circles), next-nearest (blue line, circles) neighbors within the plane, and nearest neighbors between the planes (green line with circles). The inset shows the schematics of in-plane (\parallel) nearest neighbors and next-nearest neighbors and out-of-plane (\perp) nearest neighbors. **b**, Temperature dependence of photoluminescence spectra of CrCl_3 . **c**, Temperature dependence of photoluminescence intensity. **d**, Real and imaginary parts of the complex refractive index, measured experimentally (solid lines) and calculated within the G_0W_0 approach (dotted lines). **e**, Comparison of the exciton peaks in the extinction coefficient, measured experimentally (red line) and calculated within the Bethe-Salpeter Equation (BSE) framework (blue line). **f**, Comparison of A- and B-exciton positions obtained in this work with existing works on the optical response of CrCl_3 .

Excitons in other chalcogen-based vdW crystals beyond CrCl_3

In addition to CrCl_3 , we expect a similar excitonic response for CrBr_3 and CrI_3 crystals¹⁶. However, this behavior is not limited to Cr-based vdW materials. For example, we discovered that NbOCl_2 and MoCl_3 have giant exciton binding energies, as seen in Figure 4. Indeed, their ellipsometry spectra (Supplementary Note 8 and Supplementary Note 9) demonstrate similar excitonic features as the CrCl_3 spectrum in Figure 2c. However, unlike CrCl_3 , NbOCl_2 and MoCl_3 exhibit large in-plane optical anisotropy with biaxial dielectric tensors³¹. As a result of ellipsometry fitting, we have obtained anisotropic refractive indices (Figure 4a-b) and extinction coefficients (Figure 4c-d) for NbOCl_2 and MoCl_3 . It is worth noting that a clearly separated from the bandgap excitonic peak for these materials only along one in-plane direction (Figure 4c-d). Based on Figure 4c-d, we determine the positions of excitons ($E_{\text{exciton}}^{\text{NbOCl}_2} = 1.84$ eV and $E_{\text{exciton}}^{\text{MoCl}_3} = 1.55$ eV) and corresponding bandgaps ($E_g^{\text{NbOCl}_2} = 2.50$ eV and $E_g^{\text{MoCl}_3} = 1.90$ eV). Therefore, binding energies can be found as $E_{\text{binding}}^{\text{NbOCl}_2} = E_{\text{exciton}}^{\text{NbOCl}_2} - E_g^{\text{NbOCl}_2} =$

0.66 eV and $E_{\text{binding}}^{\text{MoCl}_3} = E_{\text{exciton}}^{\text{MoCl}_3} - E_g^{\text{MoCl}_3} = 0.35$ eV. Although these values are smaller than for CrCl_3 ($E_{\text{binding}}^{\text{CrCl}_3} = 1.64$ eV), they are still colossal compared to other excitonic materials.

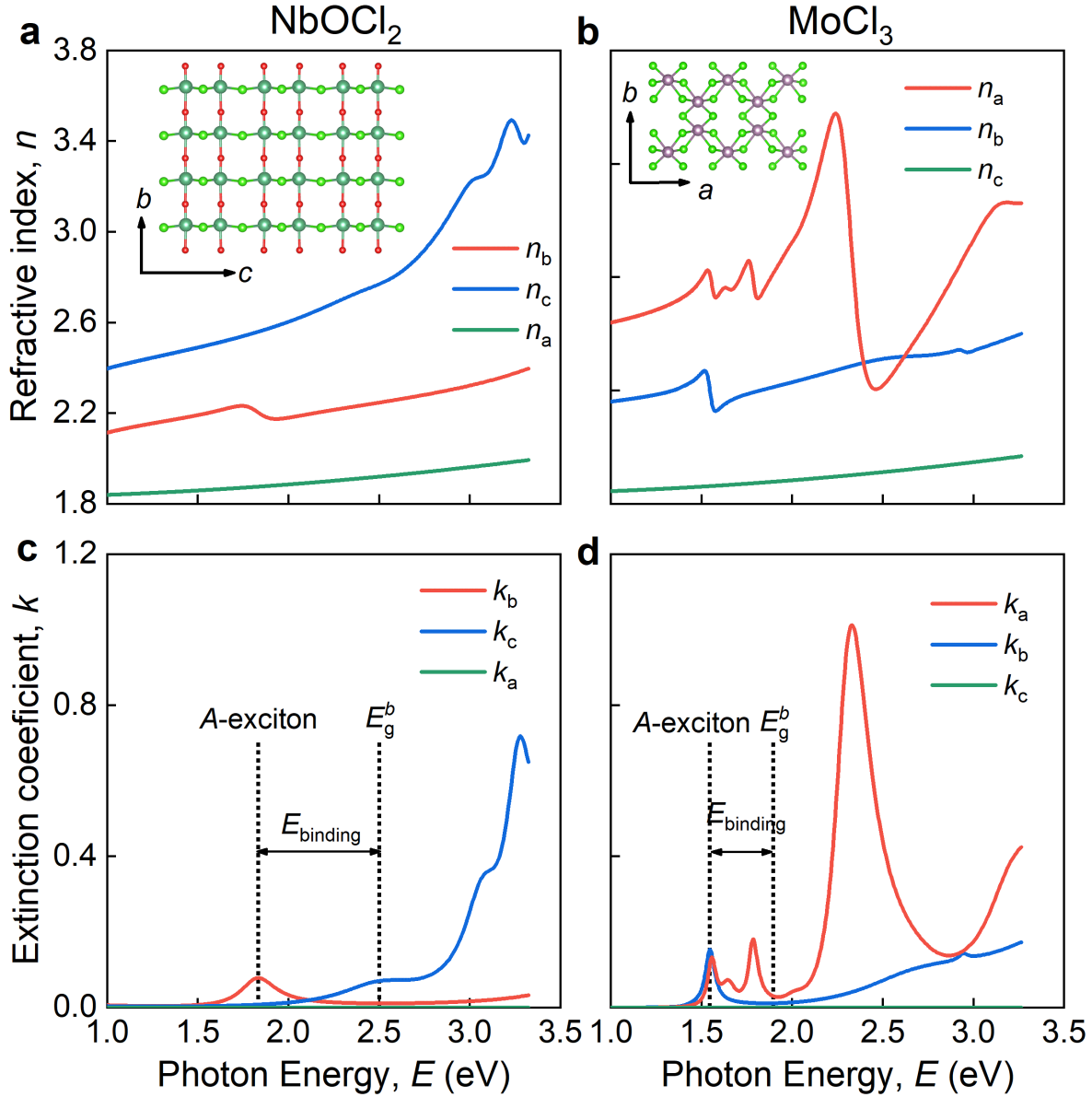


Figure 4. Layered crystals with giant exciton binding energies. The refractive index of **a**, NbOCl₂ and **b**, MoCl₃. The inset shows the crystal structure of these materials. Extinction coefficient of **c**, NbOCl₂, and **d**, MoCl₃.

Quasi-two-dimensional excitons in vdW crystals

Given these record values, it is instructive to provide a more comprehensive comparison of binding energies since, for example, the bandgap is a crucial parameter that determines exciton binding energy, as seen from the correlation of classical 3D excitonic materials in Figure 5³². Obviously, a larger bandgap generally results in larger exciton binding energy (Figure 5). If we place the results for CrCl₃, NbOCl₂, and MoCl₃ alongside monolayers MoS₂¹⁴ and WS₂¹⁵ on the same graph, we can notice that their binding energies are comparable to each other. Still, they are definitely larger than those for standard 3D excitonic materials. Of immediate interest is bulk MoS₂¹², which is in between the classical “3D exciton” region and our “2D exciton” region. This effect most likely originates from the high dielectric permittivity of 3D MoS₂ ($\epsilon \sim 16$), which effectively screens the Coulomb interaction (see the

above section “Excitons in different dimensionalities”). Furthermore, even excitons in bulk black phosphorus (BP)³³ and TiS₃ crystal³⁴ ideally correlate with other vdW materials, as seen in Figure 5. As a result, the comparison in Figure 5 reveals that excitons in vdW materials show 2D-like behavior similar to their monolayer counterparts.

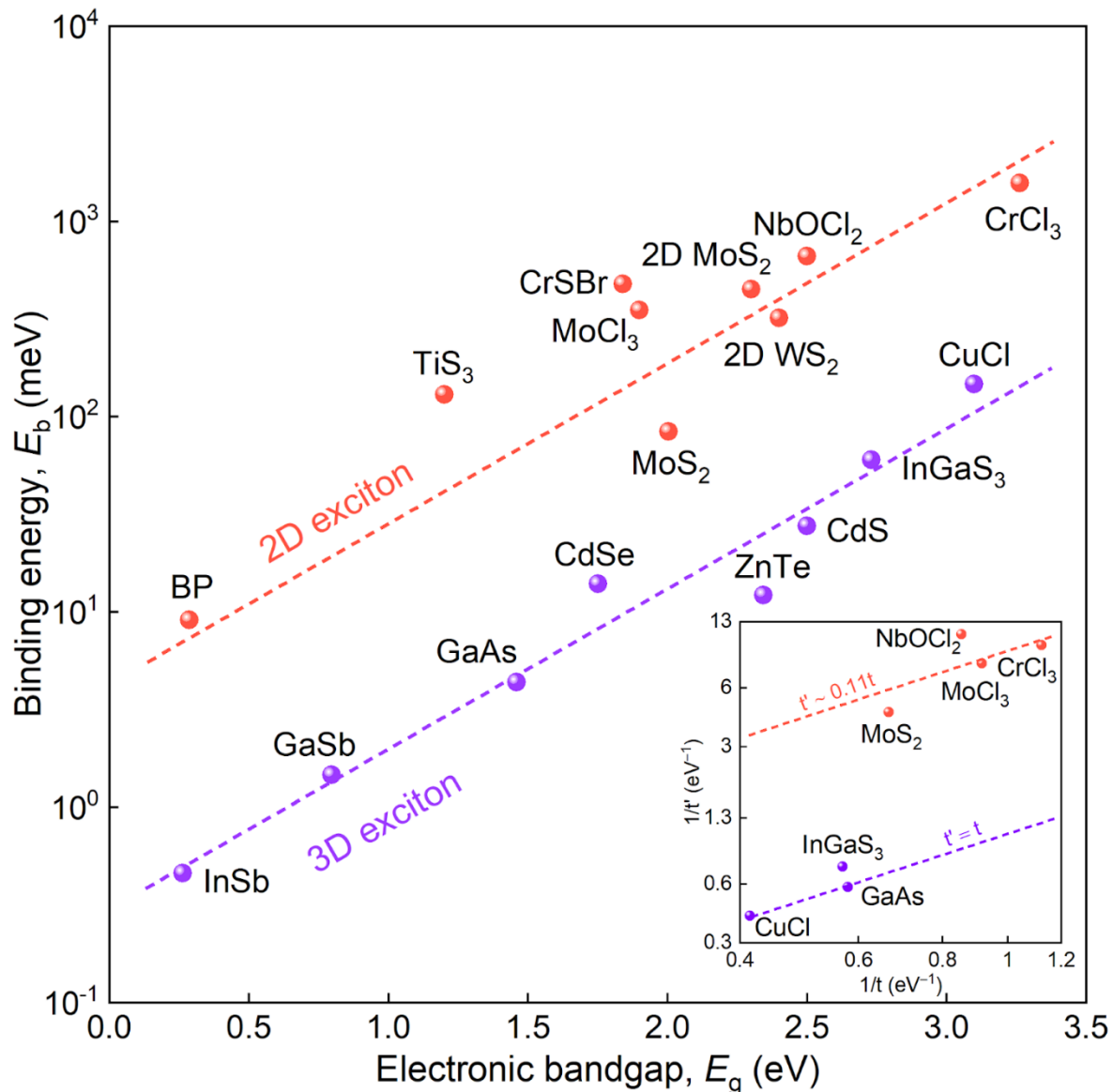


Figure 5. The comparison of 3D, 2D, and layered materials’ binding energies with respect to the corresponding bandgaps. The graph could be divided into two regions: “2D exciton” and “3D exciton”. The inset shows various compounds in the inverse intraplane ($1/t$)-inverse interplane ($1/t'$) hopping parameters coordinates.

Discussion

In summary, we positively resolved the long-standing problem of monolayer-like excitonic behavior in layered materials in the example of CrCl₃, NbOCl₂, and MoCl₃. These findings generalize the results for other vdW crystals obtained in earlier works^{12,33,34}, including BP, TiS₃, and MoS₂. Moreover, excitons in CrCl₃ result from short-order magnetic order in the crystal, offering a potential magnetic control knob of excitonic properties. Together with a facile on-chip integration of vdW crystals³⁵, it provides an unprecedented platform for exciton-integrated circuits³⁶ with numerous applications, including polaritonics³⁷, strong coupling regimes³⁸, optoelectronics³⁹, and biosensing⁴⁰.

Besides, discovered here, giant binding energies in CrCl_3 , NbOCl_2 , and MoCl_3 , combined with their low-loss optical constants, make them promising for constructing ultracompact photonic elements. For example, they could enable transparent vdW-based nanocomposites for efficient light-emitting devices⁶, optical filters⁴¹, and medical treatment⁴², especially in wearable devices, such as smart tattoos⁴³ and contact lenses⁴⁴. The characterization of the materials according to the ratio of inter- and intralayer hopping parameters can be applied also to other materials and used for computer search for new vdW materials. Therefore, our work not only provides answers of fundamental importance but also reignites interest in the excitonic properties of vdW materials beyond monolayers.

Finally, our findings establish the magnetic origin of excitons in non-magnetic CrCl_3 at room temperature. This greatly expands the rich diversity of magnetic excitons, observed in CrSBr ^{45–47}. Therefore, we anticipate corresponding phenomena for CrCl_3 , including magnetically confined surface excitons⁴⁵, magnetically controlled transport⁴⁶, hyperbolic exciton–polariton⁴⁷, and manipulation of Coulomb interaction using magnetic order⁴⁸. As a result, our work unveils the unique material platform to create and control nanoscale quantum phenomena in vdW materials.

Author Contributions

G.E. and T.M. contributed equally to this work. G.E., G.T., A.V., A.A., S.Z., A.K., K.S.N., and V.S.V. suggested and directed the project. G.A., A. Minnekhanov, G.T., A.S., A.P.Ts., M.T., M.K., N.P., A. Mazitov, A. Melentev, E.Z., and D.G. performed the measurements and analyzed the data. T.M., A.M., I.K., and A.K. provided theoretical support. G.E., T.M., A. Mazitov, and A.K. wrote the original manuscript. All authors reviewed and edited the paper. All authors contributed to the discussions and commented on the paper.

Competing Interests

The authors declare no competing financial interest.

Acknowledgements

The authors thank Dr. Valentyn Colovey for the help in preparation of manuscript's figures.

Methods

Theory. Theoretical results on the optical properties of CrCl_3 were obtained within the BSE@GW framework using VASP code⁴⁹. We used the experimentally characterized crystal structure with the lattice parameters of $a = 0.59588$ nm, $b = 1.0206$ nm, $c = 0.61138$ nm, $\alpha = 90^\circ$, $\beta = 108.495^\circ$, $\gamma = 90^\circ$ from reference²³. The exchange-correlation effects of the electrons in the DFT run were described within the Perdew–Burke–Ernzerhof functional. The behavior of the core electrons was modeled with the projector-augmented wave GW-type pseudopotentials⁵⁰. The first Brillouin zone was sampled with the Γ -centered $6 \times 4 \times 6$ mesh. The cutoff energy of the plane waves basis set was 400 eV. We considered three different variations of the Cr spins ordering: ferromagnetic (FM), with the out-of-plane (OOP FM) and the in-plane (IP FM) direction, and so-called A-type antiferromagnetic (AFM) ordering¹⁸ with interlayer AFM spin order and intralayer in-plane FM order. All theoretical calculations started with the non-collinear density functional theory (DFT) run with spin-orbit interaction taken into account to obtain the initial Kohn–Sham orbitals. The convergence threshold of the DFT self-consistent cycle was 10^{-8} eV. Next, we estimated the electronic many-body correlation effects and computed the screened

Coulomb interaction kernels within the GW approximation⁵¹, and calculated the optical properties without electron-hole interaction. Finally, we calculated the excitonic effects and obtained the excitation energies by solving the Bethe–Salpeter equation (BSE)⁵². The convergence of the excitonic peaks was achieved on taking 20 occupied and 14 virtual bands in the BSE run. Due to the limitations in the treatment of vertex corrections within the self-energy calculations, while calculating the optical absorbance we performed a rigid blue-shift of the absorbance curve by 0.5 eV, following the reasoning of reference¹⁶.

For DFT+DMFT calculations we use Standard solid-state pseudopotentials (SSSP PBEsol Efficiency v1.3.067) without considering spin-orbit interaction. The convergence threshold of the DFT self-consistent cycle was 10^{-8} . The first Brillouin zone was sampled with the Γ -centered $20 \times 20 \times 20$ k -points mesh. The resulting band structures were downfolded to Cr d-orbital states and Cl p-orbital states with Wannier90 package⁵³. This also allowed us to estimate the hopping parameter t (within the layer), which was taken as the sum of the orbital-averaged contributions from the nearest atoms in the primitive cell within a layer normalized by the number of considered bonds, and the interlayer hopping t' , which was obtained as the average contribution of hopping between atoms from different layers (considering all possible combinations within primitive cell in each layer, normalized in the same way as t). Next, we estimated the electronic many-body correlation effects within the DMFT approach, realized in the iQIST package⁵⁴. Nonlocal calculation of susceptibilities was performed by solution of the Bethe-Salpeter equations²⁴ with an account of 60–80 fermionic Matsubara frequencies, including corrections to finite frequency box^{55,56}.

Raman and Atomic Force Microscopy Analysis. The angle-resolved polarized Raman (ARPR) analysis was conducted with an alpha300 RA confocal Raman-Atomic Force Microscope (WITec, Ulm, Germany). A 532 nm laser was employed with a minimal power of 0.05 mW (corresponding to a laser density of ~ 0.7 mW/ μm^2) to prevent sample damage. The ARPR spectra were recorded in 10-degree increments (36 points total) in a parallel configuration (with the polarizer aligned parallel to the analyzer). A grating of 600 lines/mm was used, and the backscattered light was collected on a back-illuminated deep depletion CCD detector cooled to -60°C , achieving a spectral resolution of ~ 1 cm^{-1} . Each acquisition had a time of 30 s, repeated 10 times at each angle. Spectra were collected using a 100 \times objective (Zeiss EC Epiplan-Neofluar, NA 0.9 DIC).

Angle-resolved polarized PL spectra were acquired with the same setup by recording the signal every 5 degrees (72 points) of laser polarizer rotation in a parallel configuration. Each spectrum was collected once with a 1 s acquisition time. Two laser sources were utilized: a 532 nm laser at 0.05 mW, yielding a laser density of ~ 0.7 mW/ μm^2 , and a 785 nm laser set to 1 mW, corresponding to a laser density of ~ 6 mW/ μm^2 . For both wavelengths, a 300 g/mm grating with a broad spectral window was used. Spectra were collected using a 100 \times objective (Zeiss EC Epiplan-Neofluar, NA 0.9 DIC).

A Linkam T96-S heating stage was employed for temperature-dependent PL measurements. In these experiments, a 532 nm laser with a power of 0.15 mW was used in conjunction with a 50 \times objective (Zeiss LD EC Epiplan-Neofluar Dic 50 \times / 0.55), resulting in a laser density of approximately 0.8 mW/ μm^2 . A grating of 300 g/mm was utilized, and each spectrum was collected with an integration time of 1 s, averaged over 5 accumulations. To ensure consistent measurements, the PL intensity at each temperature step was normalized to the intensity of the silicon Raman peak, mitigating the effects of focus shifts. The substrate temperature was monitored using a FLIR C5 thermal camera.

Spectral processing, including cosmic ray removal, background subtraction, averaging, and smoothing, was carried out using WITec Project SIX v. 6.2 software.

Atomic Force Microscopy images were recorded in a tapping mode using the WITec alpha300 RA microscope equipped with a NanoWorld ARROW-FMR probe (75 kHz, 2.8 N/m, tip radius < 10 nm).

Spectroscopic ellipsometry. Ellipsometry of CrCl₃, NbOCl₃ and MoCl₃ were performed via Accurion EP4 imaging ellipsometer in rotating compensator mode. The samples of MoCl₃ and NbOCl₂ were aligned along their crystallographic axes to eliminate intermixing of s- and p-polarizations. The measurements were done in a broad spectral range of 250–1700 nm.

Reflection and transmission microspectroscopy. Polarized microspectroscopy measurements in the visible range were performed using optical microscopes equipped with a halogen light source polarizer and analyzer. The microscope Zeiss Axio Lab.A1 with the objective “N-Achroplan” 50×/0.8 Pol M27 was utilized for transmittance measurements. For reflectance measurements, the metallurgical microscope RX50M with the objective SOPTOP MPlanFL, ×50/0.8 was used. Transmitted and reflected light were collected from an area less than <20 μm in diameter and directed to the grating spectrometer (Optosky ATP5020P) via an optical fiber (Thorlabs M92L02). A Bruker Vertex 80v Fourier transform infrared spectrometer equipped with a Hyperion 2000 microscope was employed for polarization-resolved infrared spectroscopy. Normal incidence reflection measurements were performed using a standard 15× reflective objective (NA = 0.4). The near-infrared (NIR, 900–1400 nm) setup included a halogen lamp as the light source, a CaF₂ beamsplitter, and a mercury cadmium telluride detector.

Data Availability

The datasets generated during and/or analyzed during the current study are available from the corresponding author upon reasonable request.

References

1. Raja, A. *et al.* Coulomb engineering of the bandgap and excitons in two-dimensional materials. *Nat. Commun.* **8**, 15251 (2017).
2. Wang, Z. *et al.* Evidence of high-temperature exciton condensation in two-dimensional atomic double layers. *Nature* **574**, 76–80 (2019).
3. Lopez-Sanchez, O., Lembke, D., Kayci, M., Radenovic, A. & Kis, A. Ultrasensitive photodetectors based on monolayer MoS₂. *Nat. Nanotechnol.* **8**, 497–501 (2013).
4. Withers, F. *et al.* Light-emitting diodes by band-structure engineering in van der Waals heterostructures. *Nat. Mater.* **14**, 301–306 (2015).
5. Nassiri Nazif, K. *et al.* High-specific-power flexible transition metal dichalcogenide solar cells. *Nat. Commun.* **12**, 7034 (2021).
6. Guo, Q. *et al.* Ultrathin quantum light source with van der Waals NbOCl₂ crystal. *Nature* **613**, 53–59 (2023).
7. Weissflog, M. A. *et al.* A tunable transition metal dichalcogenide entangled photon-pair source. *Nat. Commun.* **15**, 7600 (2024).
8. Rivera, P. *et al.* Valley-polarized exciton dynamics in a 2D semiconductor heterostructure. *Science* **351**, 688–691 (2016).

9. Ermolaev, G. A. *et al.* Giant optical anisotropy in transition metal dichalcogenides for next-generation photonics. *Nat. Commun.* **12**, 854 (2021).
10. Tongay, S. *et al.* Monolayer behaviour in bulk ReS₂ due to electronic and vibrational decoupling. *Nat. Commun.* **5**, 3252 (2014).
11. Jung, E. *et al.* Unusually large exciton binding energy in multilayered 2H-MoTe₂. *Sci. Rep.* **12**, 4543 (2022).
12. Saigal, N., Sugunakar, V. & Ghosh, S. Exciton binding energy in bulk MoS₂: A reassessment. *Appl. Phys. Lett.* **108**, (2016).
13. Koperski, M. *et al.* Optical properties of atomically thin transition metal dichalcogenides: observations and puzzles. *Nanophotonics* **6**, 1289–1308 (2017).
14. Ermolaev, G. A. *et al.* Broadband optical properties of monolayer and bulk MoS₂. *npj 2D Mater. Appl.* **4**, 21 (2020).
15. Chernikov, A. *et al.* Exciton Binding Energy and Nonhydrogenic Rydberg Series in Monolayer WS₂. *Phys. Rev. Lett.* **113**, 076802 (2014).
16. Acharya, S. *et al.* Real- and momentum-space description of the excitons in bulk and monolayer chromium tri-halides. *npj 2D Mater. Appl.* **6**, 33 (2022).
17. Zhu, L. & Yang, L. Quasiparticle energies and excitonic effects of chromium trichloride: From two dimensions to bulk. *Phys. Rev. B* **101**, 245401 (2020).
18. McGuire, M. A. *et al.* Magnetic behavior and spin-lattice coupling in cleavable van der Waals layered CrCl₃ crystals. *Phys. Rev. Mater.* **1**, 014001 (2017).
19. Cai, X. *et al.* Atomically Thin CrCl₃: An In-Plane Layered Antiferromagnetic Insulator. *Nano Lett.* **19**, 3993–3998 (2019).
20. Yadav, R. *et al.* Electronic excitations and spin interactions in chromium trihalides from embedded many-body wavefunctions. *npj 2D Mater. Appl.* **8**, 56 (2024).
21. McGuire, M. Crystal and Magnetic Structures in Layered, Transition Metal Dihalides and Trihalides. *Crystals* **7**, 121 (2017).
22. Lu, S. *et al.* Controllable dimensionality conversion between 1D and 2D CrCl₃ magnetic nanostructures. *Nat. Commun.* **14**, 2465 (2023).
23. Morosin, B. & Narath, A. X-Ray Diffraction and Nuclear Quadrupole Resonance Studies of Chromium Trichloride. *J. Chem. Phys.* **40**, 1958–1967 (1964).
24. Katanin, A. A., Belozherov, A. S., Lichtenstein, A. I. & Katsnelson, M. I. Exchange interactions in iron and nickel: DFT+DMFT study in paramagnetic phase. *Phys. Rev. B* **107**, 235118 (2023).
25. Katanin, A. A., Kampf, A. P. & Irkhin, V. Y. Anomalous self-energy and Fermi surface quasisplitting in the vicinity of a ferromagnetic instability. *Phys. Rev. B* **71**, 085105 (2005).
26. Nomura, Y., Sakai, S. & Arita, R. Fermi Surface Expansion above Critical Temperature in a Hund Ferromagnet. *Phys. Rev. Lett.* **128**, 206401 (2022).
27. Liu, M. *et al.* Suppression of temperature quenching in perovskite nanocrystals for efficient and thermally stable light-emitting diodes. *Nat. Photonics* **15**, 379–385 (2021).
28. Kalytchuk, S., Zhovtiuk, O., Kershaw, S. V., Zbořil, R. & Rogach, A. L. Temperature-Dependent Exciton and Trap-Related Photoluminescence of CdTe Quantum Dots Embedded in a NaCl

- Matrix: Implication in Thermometry. *Small* **12**, 466–476 (2016).
29. Pollini, I. Electron correlations and hybridization in chromium compounds. *Solid State Commun.* **106**, 549–554 (1998).
 30. Abramchuk, M. *et al.* Controlling Magnetic and Optical Properties of the van der Waals Crystal $\text{CrCl}_{3-x}\text{Br}_x$ via Mixed Halide Chemistry. *Adv. Mater.* **30**, 1801325 (2018).
 31. Guo, Q. *et al.* Colossal in-plane optical anisotropy in a two-dimensional van der Waals crystal. *Nat. Photonics* **18**, 1170–1175 (2024).
 32. Toksumakov, A. N. *et al.* High-refractive index and mechanically cleavable non-van der Waals InGaS_3 . *npj 2D Mater. Appl.* **6**, 85 (2022).
 33. Carré, E. *et al.* Excitons in bulk black phosphorus evidenced by photoluminescence at low temperature. *2D Mater.* **8**, 021001 (2021).
 34. Molina-Mendoza, A. J. *et al.* Electronic Bandgap and Exciton Binding Energy of Layered Semiconductor TiS_3 . *Adv. Electron. Mater.* **1**, 1500126 (2015).
 35. Migliato Marega, G. *et al.* Logic-in-memory based on an atomically thin semiconductor. *Nature* **587**, 72–77 (2020).
 36. Jiang, Y., Chen, S., Zheng, W., Zheng, B. & Pan, A. Interlayer exciton formation, relaxation, and transport in TMD van der Waals heterostructures. *Light Sci. Appl.* **10**, 72 (2021).
 37. Wehmeier, L. *et al.* Tunable Phonon Polariton Hybridization in a Van der Waals Hetero-Bicrystal. *Adv. Mater.* **36**, 2401349 (2024).
 38. Canales, A., Kotov, O. & Shegai, T. O. Perfect Absorption and Strong Coupling in Supported MoS_2 Multilayers. *ACS Nano* **17**, 3401–3411 (2023).
 39. Gonzalez Marin, J. F., Unuchek, D., Watanabe, K., Taniguchi, T. & Kis, A. MoS_2 photodetectors integrated with photonic circuits. *npj 2D Mater. Appl.* **3**, 14 (2019).
 40. Oh, S.-H. *et al.* Nanophotonic biosensors harnessing van der Waals materials. *Nat. Commun.* **12**, 3824 (2021).
 41. Salih, A. E. & Butt, H. Multifunctional transition and temperature-responsive contact lenses. *Light Sci. Appl.* **12**, 271 (2023).
 42. Yan, Z. *et al.* Highly stretchable van der Waals thin films for adaptable and breathable electronic membranes. *Science* **375**, 852–859 (2022).
 43. Hlukhova, H., Kireev, D., Offenhäusser, A., Pustovyi, D. & Vitusevich, S. Graphene Field-Effect Transistors toward Study of Cardiac Ischemia at Early Stage. *Adv. Electron. Mater.* **11**, 2400332 (2025).
 44. Mironov, M. S. *et al.* Graphene-Inspired Wafer-Scale Ultrathin Gold Films. *Nano Lett.* **24**, 16270–16275 (2024).
 45. Shao, Y. *et al.* Magnetically confined surface and bulk excitons in a layered antiferromagnet. *Nat. Mater.* **24**, 391–398 (2025).
 46. Telford, E. J. *et al.* Coupling between magnetic order and charge transport in a two-dimensional magnetic semiconductor. *Nat. Mater.* **21**, 754–760 (2022).
 47. Ruta, F. L. *et al.* Hyperbolic exciton polaritons in a van der Waals magnet. *Nat. Commun.* **14**, 8261 (2023).

48. Liebich, M. *et al.* Controlling Coulomb correlations and fine structure of quasi-one-dimensional excitons by magnetic order. *Nat. Mater.* **24**, 384–390 (2025).
49. Kresse, G. & Furthmüller, J. Efficient iterative schemes for ab initio total-energy calculations using a plane-wave basis set. *Phys. Rev. B* **54**, 11169–11186 (1996).
50. Kresse, G. & Joubert, D. From ultrasoft pseudopotentials to the projector augmented-wave method. *Phys. Rev. B* **59**, 1758–1775 (1999).
51. Shishkin, M. & Kresse, G. Implementation and performance of the frequency-dependent GW method within the PAW framework. *Phys. Rev. B* **74**, 1–13 (2006).
52. Sander, T., Maggio, E. & Kresse, G. Beyond the Tamm-Dancoff approximation for extended systems using exact diagonalization. *Phys. Rev. B* **92**, 045209 (2015).
53. Pizzi, G. *et al.* Wannier90 as a community code: new features and applications. *J. Phys. Condens. Matter* **32**, 165902 (2020).
54. Huang, L. *et al.* iQIST: An open source continuous-time quantum Monte Carlo impurity solver toolkit. *Comput. Phys. Commun.* **195**, 140–160 (2015).
55. Katanin, A. Improved treatment of fermion-boson vertices and Bethe-Salpeter equations in nonlocal extensions of dynamical mean field theory. *Phys. Rev. B* **101**, 035110 (2020).
56. Katanin, A. A. Generalized dynamical mean-field theory of two-sublattice systems with long-range interactions and its application to study charge and spin correlations in graphene. *Phys. Rev. B* **104**, 245142 (2021).